1D Electronic Flat Bands in Untwisted Moiré Superlattices

*Yafei Li, Qing Yuan, Deping Guo, Cancan Lou, Xingxia Cui, Guangqiang Mei,
Hrvoje Petek, Limin Cao, Wei Ji,* and Min Feng**

After the preparation of 2D electronic flat band (EFB) in van der Waals (vdW) superlattices, recent measurements suggest the existence of 1D electronic flat bands (1D-EFBs) in twisted vdW bilayers. However, the realization of 1D-EFBs is experimentally elusive in untwisted 2D layers, which is desired considering their fabrication and scalability. Herein, the discovery of 1D-EFBs is reported in an untwisted in situ-grown two atomic-layer Bi(110) superlattice self-aligned on an SnSe(001) substrate using scanning probe microscopy measurements and density functional theory calculations. While the Bi–Bi dimers of Bi zigzag (ZZ) chains are buckled, the epitaxial lattice mismatch between the Bi and SnSe layers induces two 1D buckling reversal regions (BRRs) extending along the ZZ direction in each Bi(110)-11 × 11 supercell. A series of 1D-EFBs arises spatially following BRRs that isolate electronic states along the armchair (AC) direction and localize electrons in 1D extended states along ZZ due to quantum interference at a topological node. This work provides a generalized strategy for engineering 1D-EFBs in utilizing lattice mismatch between untwisted rectangular vdW layers.

1. Introduction

Correlated electronic quantum phenomena in low-dimensional materials and their engineered superstructures are of fundamental interest[1–6] and technological importance[7–12] for the discovery and application of novel quantum materials. Homo- and hetero-bilayers of graphene,[2,13–19] transition-metal dichalcogenides (TMDs),[3–5,8,20–26] and related materials[1,7,27] have been stacked at defined twisting angles[1–5,7,8,12–17,19–24,27] or with a small lattice mismatch[25] to form 2D moiré superlattices with underlying hexagonal/triangular symmetry. This creates 2D isotropic flat bands and triggers electron correlation by subtly tuning the in-plane kinetic energy and thereby the interactions among carriers. Thus, they are attractive platforms with unprecedented potential[28,29] for exploring collective electronic states of matter, such as correlated insulators,[2,4,22,23,27] Wigner crystals,[3] and pair density waves in high-temperature superconductors.[13,14,19,21]

Following the standard approach to achieve 2D isotropic flat bands through modification of the relative twist angle between combined sheets,[2,4,14,15,17–19,22–25,27] recent studies have unveiled 1D correlated phenomena in twisted bilayer moiré systems.[5,9] 1D strain-induced moiré potentials and the related excitons were demonstrated in twisted $WSe_2/MoSe_2$ TMDs hetero-bilayers.[9] 1D Luttinger liquid states emerge in the moiré superlattice of the twisted anisotropic WTe_2 homo-bilayer.[5] More strikingly, 1D electronic flat bands (1D-EFBs) have been predicted to exist in twisted anisotropic 2D crystals such as GeSe[30] and SnS.[31] Considering the technological challenge of delicately controlling the twisting angles between atomic layers, an approach that relies on building untwisted moiré superlattices that intrinsically host 1D-EFBs seems more feasible. Such an approach has not currently been experimentally realized or even theoretically proposed.

Herein, we report the experimental realization of 1D-EFBs in an untwisted but lattice-mismatched anisotropic hetero-bilayer. Through van der Waals (vdW) epitaxy, we grew rectangular, two atomic layer-thick (2-AL) Bi(110) on an SnSe(001) substrate. The epitaxial lattice mismatch between the Bi and SnSe lattices led to the formation of a rectangular Bi(110)-11 × 11/SnSe(001)-12 × 12 moiré superlattice. In particular, in the Bi(110)-11 × 11 supercell, the lattice mismatch in the armchair (AC) direction flips the buckling direction of Bi-Bi dimers in Bi zigzag (ZZ) chains, leading to the formation of two stripe-like buckling reversal regions (BRRs) in each supercell. We characterized the atomic

Y. Li, Q. Yuan, C. Lou, X. Cui, G. Mei, L. Cao, M. Feng
School of Physics and Technology and Key Laboratory
of Artificial Micro- and Nano-Structures of Ministry of Education
Wuhan University
Wuhan 430072, P. R. China
E-mail: fengmin@whu.edu.cn

D. Guo, W. Ji
Beijing Key Laboratory of Optoelectronic Functional Materials &
Micro-Nano Devices
Department of Physics
Renmin University of China
Beijing 100872, P. R. China
E-mail: wji@ruc.edu.cn

D. Guo, W. Ji
Key Laboratory of Quantum State Construction and Manipulation
(Ministry of Education)
Renmin Universiry of China
Beijing 100872, P. R. China

H. Petek
Department of Physics and Astronomy and the IQ Initiative
University of Pittsburgh
Pittsburgh 15260, USA

M. Feng
Institute for Advanced Study
Wuhan University
Wuhan 430072, P. R. China
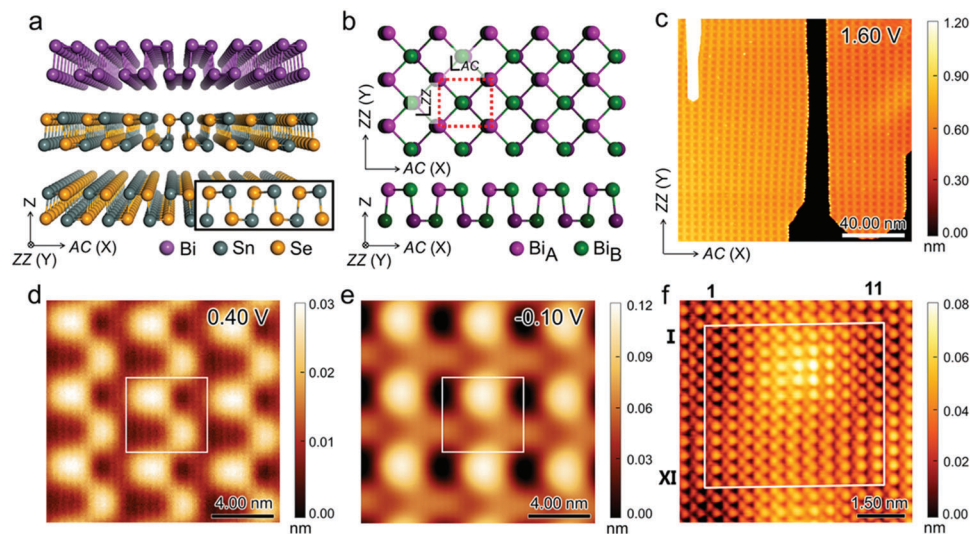
Figure 1. 2-AL Bi(110) superlattice on SnSe(001). a) Side view of a structural model of an aligned, noninteracting Bi/SnSe interface. b) Top and cross-sectional views of the model of an isolated 2-AL Bi(110) layer with Bi_A and Bi_B atoms shown in purple and green, respectively, in the top and bottom atomic layers. The red dotted rectangle defines the layer unit cell. c) STM image of Bi islands grown on the SnSe substrate. d,e) Two typical STM images acquired at +0.40 V ($I = 20$ pA) and −0.10 V ($I = 20$ pA), respectively. The white rectangle represents the supercell, which reveals a contrast shift between (d) and (e). f) Atom-resolved STM image of the Bi(110) supercell (0.14 V and 100 pA) with the white rectangle indicating the supercell shown in (d) and (e). The supercell was composed of 11 ZZ chains and 11 AC rows, which are marked by the numbers 1–11 and I–XI, respectively.

structures of the buckling reversal (BR) Bi chains in the Bi(110) supercell via qPlus non-contact atomic force microscopy (qPlus nc-AFM) measurements and density functional theory (DFT) calculations. Scanning tunnelling microscopy/spectroscopy, together with DFT calculations, revealed several 1D-EFBs around the E_F. Through microscopic subatomic-resolution imaging of the moiré relaxation and electronic characterization of the resulting flat bands, we discovered that the spatial distribution of the electron density (wavefunction norms ($|\psi|^2$)) of these flat bands was nearly superposed on the experimentally (and theoretically) revealed BR stripes. Moreover, the local geometry of BRRs was found to determine whether a 1D-EFB is a bonding or an antibonding state. The two BRRs in each supercell have topologically opposite geometries, which separate those observed 1D-EFBs spatially and energetically. Given the correlation of the lattice mismatch-induced BR structures and the 1D flat bands they host, our work establishes a strategy for the scalable design of novel 1D quantum states in untwisted 2D moiré superlattices.

2. Results and Discussion

### 2.1. Bi(110)-11 × 11/SnSe(001)-12 × 12 Superlattice

Figure 1a presents a schematic model of a 2-AL Bi(110) layer above an SnSe(001) substrate. SnSe(001) is a structural analogue of black phosphorous (BP)[32–34] composed of 2-AL Sn–Se pairs, except that the Sn atoms are slightly elevated over the plane of neighboring Se atoms (Figure 1a).[35–37] The Bi(110) layer also has a BP-like structure, which is composed of 2-AL Bi zigzag chains, as shown in Figure 1b.[38–40] In each AL, a unit cell of Bi (red dashed rectangle in Figure 1b) contains two Bi atoms (denoted as Bi_A–Bi_B), forming a Bi–Bi dimer which is unpuck-

ered on isotropic substrates such as highly oriented pyrolytic graphite.[41,42]

A typical STM image (Figure 1c) of an as-grown Bi(110) film exhibited waffle-like rectangular superstructures. Magnified images acquired under positive (0.40 V, see Figure 1d) and negative (−0.10 V, Figure 1e) biases exhibited different contrast distributions. According to the STM contrast at a positive bias and atom-resolved structure, we identified a supercell in the Bi superstructure (Figure 1d,f). The size of the supercell was ≈53.7 Å (AC) × 50.1 Å (ZZ), corresponding to an 11 × 11 Bi(110) unit cell with the measured Bi(110) lattice constants of 4.8 ± 0.2 (AC) and 4.5 ± 0.2 (ZZ) Å. In total, 11 atomic chains extending in both the ZZ and AC directions in each supercell (indicated by the white solid rectangle) were observed in the atom-resolved STM image shown in Figure 1f, which explicitly verified this 11 × 11 supercell. An STM image of an edge of the Bi island (Figure S1, Supporting Information) indicated that this Bi 11 × 11 superlattice was untwisted with respect to the SnSe substrate. Therefore, we concluded that the Bi layer formed a Bi-11 × 11/SnSe-12 × 12 moiré superlattice, given the observed alignment between Bi and SnSe and the measured SnSe lattice constants of 4.5 ± 0.2 (AC) and 4.2 ± 0.2 (ZZ) Å.

2.2. Atomic Structure of the Buckling Reversal for Bi atomic Chains

As the appearance of the supercell varied significantly under different bias voltages (Figure S2, Supporting Information), we characterized the Bi atomic structure using qPlus nc-AFM, which enables recording surface geometry with minimal electronic effects. A point defect on the Bi surface (Figure S3, Supporting

**ADVANCED
SCIENCE NEWS**

www.advancedsciencenews.com

**ADVANCED
MATERIALS**

www.advmat.de
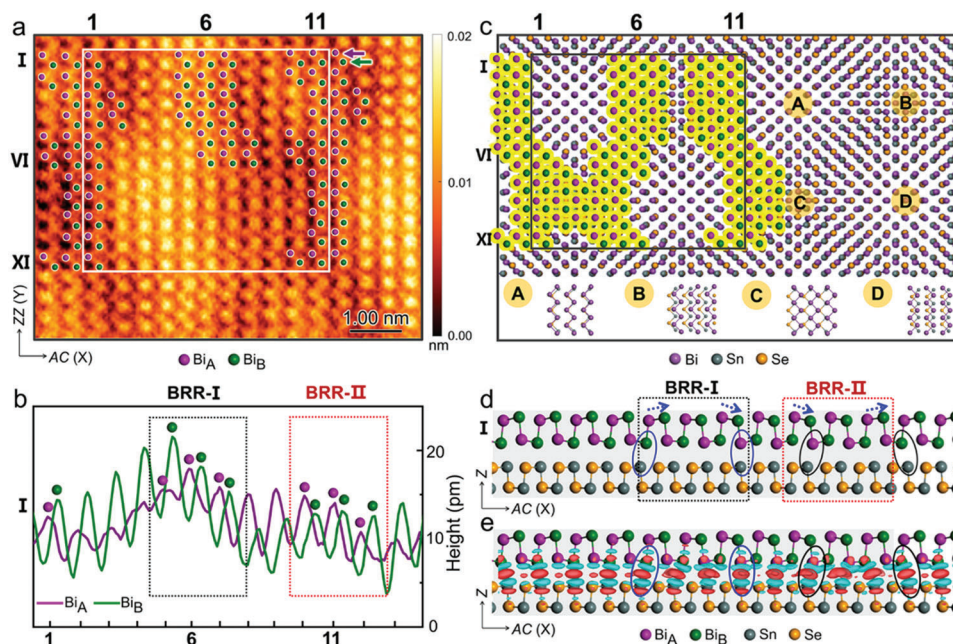
Figure 2. Experimentally and theoretically established buckling atomic structures of Bi(110) supercell. a) Atomic-resolution constant Δf mode qPlus AFM image (CO tip, $\Delta f = -3.85$ Hz). The purple and green dots represent Bi_A–Bi_B pairs, which indicate the spatial positions of BRRs. Other markers displayed in panels (b) and (c) have identical meanings to those in panel (a). b) Line profiles cutting along Bi_A and Bi_B atoms marked by the purple and green arrows in (a) in the AC direction. The black (red) dotted rectangle denotes BRR-I (-II), where the atomic buckling directions are reversed. The purple and green dots denote the atomic positions and heights of the Bi_A and Bi_B atoms, respectively. c) Atomic model of the relaxed $11L_{AC} \times 11L_{ZZ}$ 2-AL Bi(110) on SnSe(001). The typical stacking configurations are presented. The dark grey rectangle marks the confirmed supercell corresponding to the experimentally established one in (a). d) Side view of the AC row I in the supercell in (c). The black (red) dotted rectangle marks the theoretical BRR-I (-II). The blue arrows indicate the buckling direction of the Bi_A–Bi_B pair. The spatial distributions of BRRs are demonstrated by highlighting the BRR-involved Bi_A–Bi_B pairs with yellow in (c). e) Interfacial charge density exhibits changes in the interacting atomic pairs in the BRRs, highlighted by the ovals in (d) and (e). The rectangular grey shading in (d), and (e) denotes the lateral dimension of one supercell.

Information) allowed us to precisely correlate the positions of the image contrasts observed in AFM and STM.

Figure 2a presents an atom-resolved nc-AFM image showing the vertical positions of each Bi_A and Bi_B atom on the surface, which clearly indicates the atomic height variations. Figure 2b shows the apparent height variations for the row I of the Bi_A and Bi_B atoms (purple and green markers, respectively) from columns 1–11. The apparent heights of the Bi_B and Bi_A rows (green and purple curves, respectively) had similar distributions that varied within ≈10 pm. Remarkably, the two height variation curves were not synchronous. In particular, within columns 1–6, the apparent height of each Bi_A atom was lower than that of the corresponding Bi_B atom. However, in columns 6–11, the relative height order of the Bi_A-Bi_B pairs was reversed with a transition region at column 6, where the apparent heights of the Bi_A and Bi_B atoms were nearly equal, as indicated by the black dotted rectangle in Figure 2b. Another BR process occurred but in the opposite reversal direction, in the same row at column 11 (red dotted rectangle). To distinguish the reversed BR structures according to their buckling directions, we named the former BR region BRR-I and the latter BRR-II. BRR-I represents the buckling transition from the right-up direction, for the Bi_A–Bi_B vector (purple-green), to the right-down direction. BRR-II represents the transition from the right-down to the right-up direction. By examining the AC rows one by one in the Bi 11 × 11 supercell (Figure S4, Supporting Information) we discovered that the

two BR processes repeated throughout the supercell. BRR-I was primarily observable in a curved region around column 6 from rows I–VI, while BRR-II was detectable within a ZZ-like region around column 11 for most rows. We superpose the spatial distribution of the two BRRs with atomic positions on the AFM image in Figure 2a. Through atomically resolved AFM imaging, we directly recorded the atom relaxation-induced fine structures in the moiré superlattice, whereas in previous studies, indirect evidence of their existence was obtained.[25]

Our DFT calculations reproduced the BR features in the Bi/SnSe supercell well. Figure 2c presents the fully relaxed atomic structures of the Bi-11 × 11/SnSe-12 × 12 hetero-bilayers, which contain four typical stacking orders, as shown in the insets. The supercell marked by the dark grey rectangle was determined by comparing the spatial distributions of experimentally observed and theoretically revealed BRRs and wavefunction norms ($|\psi|^2$) at certain energies, as discussed later. A side view of row I is presented in Figure 2d, clearly showing the BRR-I (-II) structure at the middle (edge) of the supercell, as highlighted by the black (red) dotted rectangle. As shown in Figure 2e, the substrate Sn atom has a wavefunction overlap with the elevated Bi atoms, which change from Bi_B (Bi_A) on the left side of BRR-I (-II) to Bi_A (Bi_B) on the right side, as indicated by the blue (black) ovals. This change of the interlayer close-contact atomic pairs leads to the BR and is a result of mismatch lattices between Bi and SnSe in the AC direction. By repeating the procedure used for the AFM
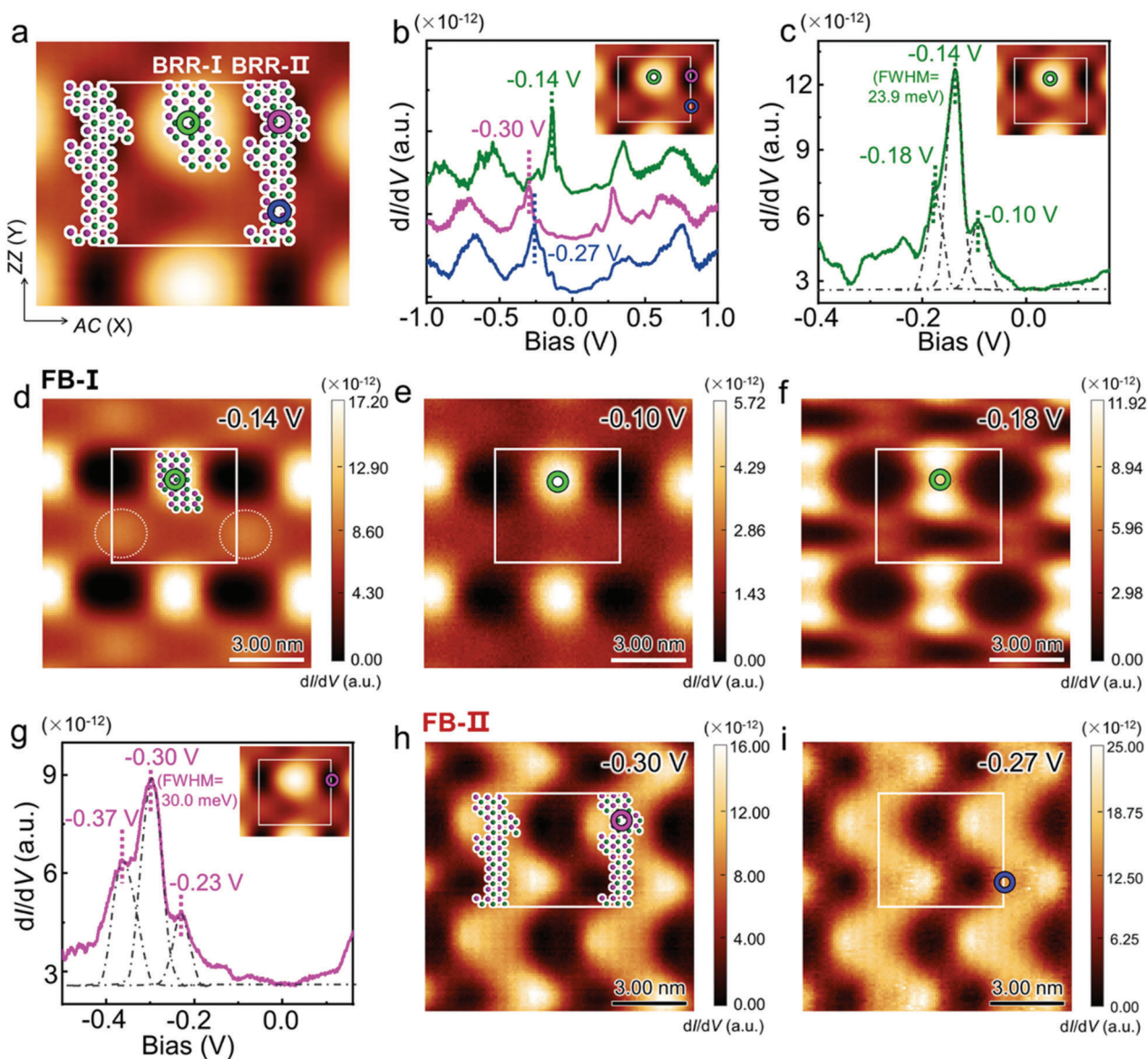
Figure 3. Experimentally quantified 1D-FEBs in Bi(110) superlattice on SnSe(001). a) Typical STM image acquired at −0.10 V superposed with the spatial distribution of the BRRs based on an atomic model of Bi_A–Bi_B pairs. The circles mark the centers of the BRRs. The white rectangle marks one supercell. b) Typical STS dI/dV spectra acquired around the sites marked by the green, pink, and blue circles in (a) and in the inset STM image. c) Zoomed-in STS spectrum recorded at the green circle location (inset) with the analysis of the −0.14 V peak. d–f) STS dI/dV maps obtained at the energies of the −0.14, −0.10, and −0.18 V spectral components in (c), respectively. The spatial distribution of BRR-I is marked in (d). g) Zoomed-in STS dI/dV spectrum acquired from the pink circle location (inset) with the analysis of the −0.30 V peak. h) STS dI/dV map obtained at −0.30 V from (g). The spatial distribution of BRR-II is superposed on the STS image in (h). i) STS dI/dV map obtained at −0.27 V from (b).

images (Figure S5, Supporting Information), we found that the theoretical BR distributions had a comparable pattern to those observed in the AFM images (see Figure 2c, highlighted yellow), which, again, indicates the existence of BRs.

2.3. Experimentally Observed 1D Flat Bands

The previously suggested importance of the atomic relaxation to 2D flat bands aside,[25,43] we demonstrated that the BR introduced 1D-EFBs in our Bi/SnSe hetero-bilayers. **Figure 3**a presents the

spatial distribution of BRR-I (-II) in the STM image acquired at −0.10 V, where three circles mark the typical locations within the BR regions. Figure 3b presents the STS dI/dV spectra corresponding to Figure 3a. At the center of BRR-I (green circle in Figure 3a,b), the STS spectrum exhibits a pronounced narrow peak at −0.14 V which substantially weakens at the upper (pink circle) and lower (blue circle) parts of BRR-II, where sharp peaks appear at −0.30 and −0.27 V, respectively.

Figure 3c shows a magnified dI/dV spectrum of the −0.14 V peak measured at the centre of BRR-I. The extracted full width at half maximum (FWHM) for this peak was between 23 and 30 mV

**ADVANCED
SCIENCE NEWS**

www.advancedsciencenews.com

**ADVANCED
MATERIALS**

www.advmat.de

at $T = 5.0$ K, weakly depending on the modulation voltage used in the measurements (Figure S6, Supporting Information).[44] A sharp STS peak has previously been established as evidence for 2D electronic flat bands.[24,25,43,45] Our observed FWHM is comparable to those previously reported FWHM values of several to 40 mV for 2D electronic flat bands in twisted bilayer graphene,[16,17,19] and ≈ 12 mV in untwisted WSe_2/WS_2 stacked layers.[25] Therefore, we refer this state as FB-I. The STS map at this energy (Figure 3d) exhibited a pronounced high-density area around BRR-I, where an atomic model is superposed, with two far less bright regions located slightly asymmetrically below it (marked by the two white dotted circles). Detailed STS spectra near the high-density area indicate that the intensity of FB-I abruptly decreases away from the centre of the area (Figure S7, Supporting Information), indicating that this state is spatially localised in the *AC* direction. Similar spatial localisations as characteristic features of flat bands have been observed in graphene and TMD-based moiré superlattices.[25,43,45]

In addition, FB-I had (at least) two dominant "satellite" peaks with maxima at -0.10 and -0.18 V, as shown in Figure 3c. The -0.10 V state in Figure 3e exhibits a comparable spatial distribution to FB-I. While the -0.18 V state, shown in Figure 3f, has a "dumbbell-like" pattern with a node at the green spot. These observed spatial distributions for the FB-I (-0.14 V) and the -0.18 V state are reminiscent of the quantum series of the 2D flat bands in an effective moiré potential.[24,25,43,45] For example, the characteristic STS maps at flat band energies in WSe_2/WS_2 superlattice presented a strong solid contrast on the $B^{Se/W}$ site, while at slightly lower energies, the formation of a node at the center of the $B^{Se/W}$ site has been demonstrated.[25] This was interpreted as another evidence of 2D flat bands. Here, three experimental signatures reported in 2D flat bands, that is, the small FWHM of the STS peak, the strong spatial localization, and the quantum series of the related electronic states were identified for FB-I, fingerprinting its flat band characteristic. However, the existence of the two dimmer regions in the STS map, indicating spatial anisotropy, differentiated FB-I from previously reported 2D flat bands that exhibited isotropic STS patterns in triangular or hexagonal moiré superlattices.[24,25,43,45] The anisotropic feature of FB-I suggests that a distinct 1D electronic state could emerge in our Bi(110) rectangular moiré superlattice, which is consistent with and reproduced by our theoretical calculations, presented below.

The FWHM of ≈ 30.0 mV for the -0.30 V peak shown in Figure 3g also indicated its EFB nature. We refer to this state as FB-II. However, the corresponding dI/dV map at -0.30 V of FB-II state (Figure 3h) is primarily distributed following the 1D pattern of BRR-II while uniquely exhibiting a zigzag-shaped 1D distribution oriented parallel to the *ZZ* direction. The STS map for the -0.27 V peak (Figure 3i) is almost the same as that of FB-II, indicating that they have similar electronic origins. The STS map of FB-II (Figure 3h) indicates that it is spatially isolated in the *AC* direction and is propagated by and follows BRR-II, which indicates the 1D feature of FB-II. The 1D feature besides, FB-II is a 1D-EFB that its bandwidth in the direction of propagation (*ZZ*) is comparable to that in the *AC* direction. Although the small bandwidth in *AC* could be ascribed to the suppressed wavefunction overlap due to spatial isolation,[46] that in *ZZ* has other non-trivial origins as we will elucidate later. 1D-EFBs were predicted to ex-
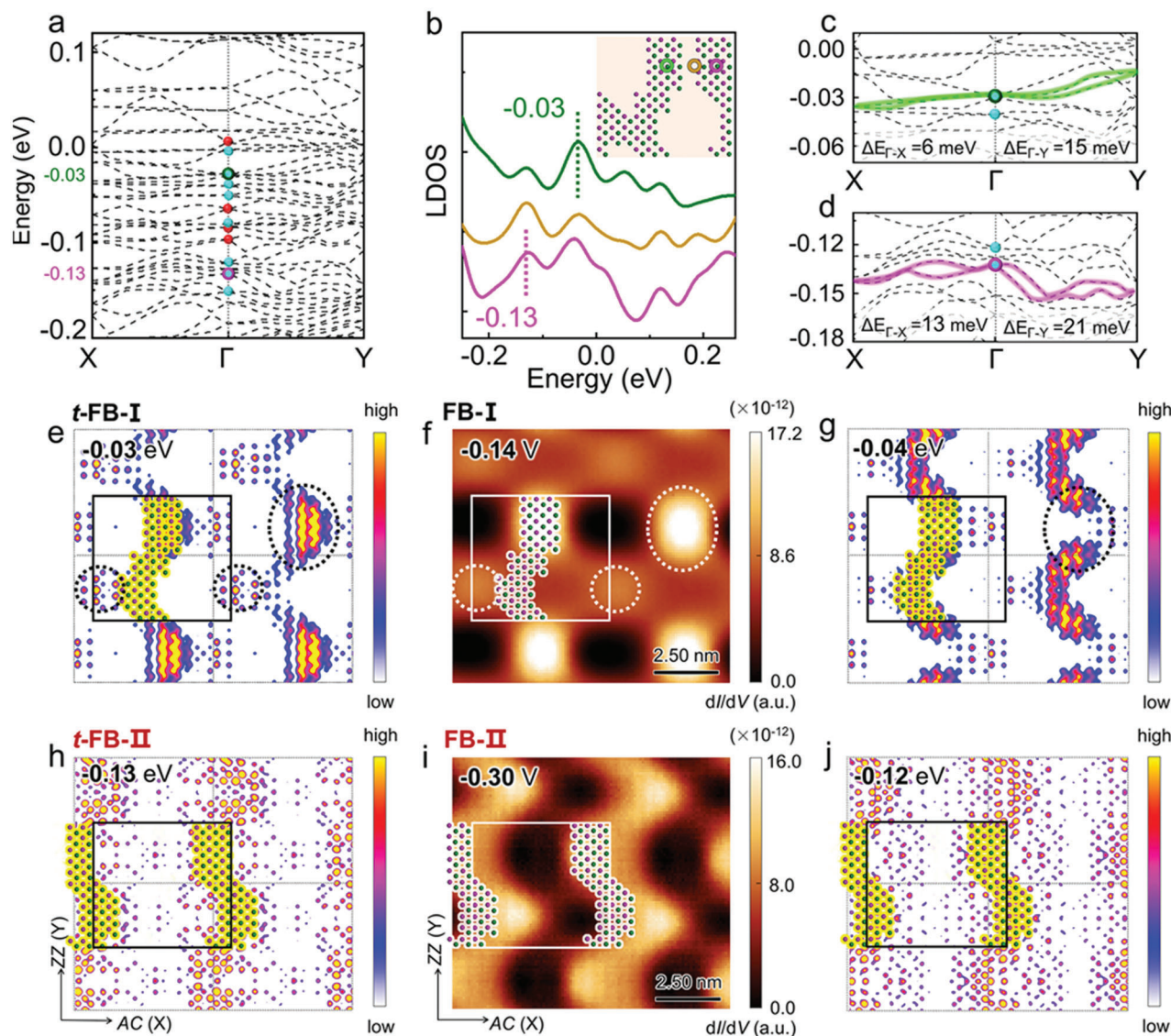
ist in twisted $GeSe$[30] and SnS[31] homo-bilayers where similar features, namely electronic localization in the propagating directions of 1D states, were shown,[30,31] verifying the 1D-EFB features of the states discovered in our untwisted Bi/SnSe heterostructure.

As that for FB-I, the FB-II peak has two primary "satellite" peaks at -0.23 and -0.37 V (Figure 3g). We acquired STS dI/dV maps at the energies of the "satellite" peaks (-0.23 and -0.37 V) of FB-II (Figure S8, Supporting Information). They show similar features to those of the -0.30 V FB-II peak, indicating they might arise from the same origin. However, no node was observed in those two satellite states (Figure S8, Supporting Information). This is different from that of FB-I. We suggest that this difference is, most likely, ascribed to different spatial density distributions of FB-I and FB-II. Our DFT simulations fully reproduced the different spatial distributions of FB-I and FB-II (see below).

2.4. DFT Modelling of the 1D-EFBs

The electronic band structure of the fully relaxed Bi-11×11/SnSe-12×12 supercell (Figure 2c) is plotted in **Figure 4**a. Many bands are nearly flat and slightly dispersive in the $\Gamma-X$ (*AC*) and $\Gamma-Y$ (*ZZ*) directions, as indicated by cyan or red dots at the Γ point. These bands have two origins: in-plane Bi p_x-p_y (red dots) and out-of-plane Bi p_z (cyan dots) orbitals, as shown in Figures S9,S10 (Supporting Information). The p_z states extend further than the p_x and p_y states from the Bi layer surface (see side views of $|\psi|^2$ in Figures S9,S10, Supporting Information). Therefore, the primary contributions to our measured STM contrast are the electronic states of the p_z bands.

By examining all the p_z (cyan dots) states of interest, we found that a state residing at -0.03 eV (marked with a green circle in Figure 4a) was the most pronounced around the high-density area of BRR-I (Figure 4b) and exhibited a comparable spatial density of states (DOS) pattern to FB-I (Figure 4e); thus, we denoted this state as theoretical FB-I (*t*-FB-I). A slightly doped SnSe substrate could explain the energy difference between FB-I (-0.14 V) and *t*-FB-I (-0.03 eV). The *t*-FB-I state fades into another p_z state centered at -0.13 eV, herein denoted as *t*-FB-II (pink circle in Figure 4a) in BRR-II. The transition of the local density of states (LDOS) peaks shown in Figure 4b appears similar to that of the STS spectra shown in Figure 3b (and also Figure S7, Supporting Information), further confirming our assignments. We note here that the LDOS spectra in Figure 4b were plotted at the Γ point, as the STS signals primarily arose from the electronic states around that point in most cases. To examine the likely contribution of those states away from the Γ point to this LDOS peak, we further plotted the electronic band structures along high-symmetry paths covering the entire 2D Brillouin zone (BZ) in Figure S11 (Supporting Information). The band structure exhibits that the maximum bandwidth of *t*-FB-I (II) is ≈ 23 (39) meV in the entire BZ, in which it is smaller than ≈ 15 (and ≈ 21) meV along the $\Gamma-X$ and $\Gamma-Y$ paths. Given the measured FWHM of 23.9 (30.0) meV for FB-I (II) states, we conclude that *t*-FB-I (II) band could, at least primarily, lead to the observed narrow STS peaks. In Figure 4c,d we show the expanded band structures of *t*-FB-I (-II), respectively, from which their bandwidths were found to be 6 (13) and 15 (21) meV along the $\Gamma-X$ and $\Gamma-Y$ directions, respectively.

ADVANCED
SCIENCE NEWS
www.advancedsciencenews.com

ADVANCED
MATERIALS
www.advmat.de

Figure 4. Theoretically quantified 1D-FEBs in Bi(110) superlattice on SnSe(001). a) Band structure of the relaxed Bi(110)-11 × 11/SnSe(001)-12 × 12 supercell. The cyan and red dots mark the dominant p_z and p_x-p_y bands, respectively. Two p_z bands at −0.03 and −0.13 eV are highlighted by cyan dots with green and pink circles according to the LDOS peaks in (b). b) Calculated location-dependent LDOS acquired from sites marked in the inset image of the theoretically established BRRs. The green and pink circles mark the same spatial locations as those in Figure 3b. c,d) Zoomed-in images showing the bandwidths along the X–Γ–Y path for the two highlighted 1D-EFBs in (a). The cyan dots mark the p_z bands close to the highlighted bands. e,h) plot 2D sections of $|\psi|^2$ of t-FB-I (-II) in the slab 2.3 Å over the top Bi layer, which is comparable to the observed STS map of FB-I (-II), as replotted in (f,i). The theoretically established spatial distribution of the BRRs is superposed on the STS maps. g,j) 2D sections of the "satellite" states of t-FB-I (-II) are depicted in (g,j). Atomic models of BRRs are superposed in (e,g,h,j). The black dotted ovals in (e) and (g) denote the position highlighted using the while-dotted oval in (f). The two white dotted circles in (f) mark two less bright spots, which correspond to the black dotted circles in (e). The black (white) rectangles indicate the size of the supercell.

These bandwidth values are similar to those reported for 2D flat bands in twisted WSe$_2$/WS$_2$ or buckled graphene superlattices, namely, several to over 20 meV,[18,25] suggesting they are of flat band characteristics. Furthermore, both bands are "flatter" along Γ–X than Γ–Y, exhibiting anisotropy in the two orthogonal directions. We also found p_z states energetically close to t-FB-I and –II in the band structure plots, marked with cyan dots in Figure 4c,d, respectively, which are merged within the main LDOS peaks of t-FB-I and -II in Figure 4b.

The spatial distribution of $|\psi|^2$ for t-FB-I (Figure 4e) reproduces the STS map of FB-I well. The highest density occurs at the position near BRR-I (yellow atomic model), as indicated by a black dotted oval, which coincides with that of the experimentally observed high-density area of FB-I (Figures 3d,4f). Moreover, the two black dotted circles in Figure 4e indicate two appreciably lower-density regions, which again reproduces the experimental observations indicated by white dotted circles in Figures 3d,4f. Figure 4g presents the density contours of the satellite state of

**ADVANCED
SCIENCE NEWS**

www.advancedsciencenews.com

**ADVANCED
MATERIALS**

www.advmat.de

t-FB-I, which exhibits similar spatial features to those of *t*-FB-I, except that a node appears in the area indicated by the black oval in Figure 4g. This difference is consistent with the experimental STS results shown in Figure 3d,f, where a node appears in the −0.18 V satellite state of FB-I (Figure 3f).

The spatial distribution of *t*-FB-II (Figure 4h) exhibits a continuous 1D striped appearance along the *ZZ* direction, nearly spatially following BRR-II (yellow atomic models). This result closely resembles the STS map observed for FB-II, as shown in Figure 4i. A satellite peak at −0.12 eV exhibits a nearly identical spatial distribution (Figure 4j) to that for *t*-FB-II at −0.13 eV. This pair of states is consistent with the experimentally observed −0.30 and −0.23 V STS peaks shown in Figure S8 (Supporting Information).

The key characteristic of *t*-FB-I and *t*-FB-II is that the spatial distribution of $|\psi|^2$ is isolated along the *AC* direction but extends one dimensionally along the *ZZ* direction. Although *t*-FB-I (-II) is propagating along *ZZ*, its 15 (21) meV bandwidth reveals that electrons are localized along this direction, confirming its nontrivial origin, consistent with our experimental observations. These characteristic features, that is, the respective localization and isolation in two orthogonal directions, are consistent with what is theoretically predicted for 1D flat band in twisted bilayer GeSe[30] and SnS,[31] identifying the 1D-EFB nature of *t*-FB-I (-II). An interesting question remains: why are *t*-FB-I and -II energetically and spatially separated? The side views of the charge densities of *t*-FB-I and -II (Figures S9,S10, Supporting Information) clearly indicate that *t*-FB-I around BRR-I is an anti-bonding state of the p_z orbitals between the two Bi atomic layers, whereas *t*-FB-II, spatially distributed around BRR-II, is a bonding one. This finding explains why the dominant STS (LODS) peaks shown in Figure 3b and Figure 4b, respectively, are separated both energetically and spatially. It also explains the energetical and spatial separations of other bands around E_F (Figures S9,S10, Supporting Information).

The BRRs are the key factor leading to 1D-EFBs, which was verified by further calculations. When we removed the BRRs and calculated the band structure using an un-relaxed atomic structure, no EFBs were found in the unrelaxed supercell (Figure S12, Supporting Information). Next, we removed the substrate and left the BRRs unchanged. Such a distorted freestanding monolayer explicitly shows many anti-bonding (bonding) 1D-EFBs around E_F in energy and BRR-I (-II) spatially (Figure S13, Supporting Information). As shown in Figure S13 (Supporting Information), the bands along Γ–*X* are completely flattened by spatial isolation in the *AC* direction, while they are more dispersive in the Γ−*Y* direction owing to electron localisation in the 1D extended states along *ZZ*, explicitly exhibiting the 1D-EFB character. However, with further removal of the BRRs, a freestanding monolayer does not exhibit any 1D-FEBs (Figure S14, Supporting Information). These results confirm that the Bi–SnSe interactions at the heterointerface induce BR structures in the Bi layer, which, rather than the electronic interactions from the substrate, essentially determine the 1D-FEBs in the Bi layer. However, the Bi-SnSe interactions lower the energies of the emergent 1D FEBs (Figure S15, Supporting Information), owing to the formation of bonding Bi–SnSe hybridized states.

3. Conclusion

Through vdW epitaxial growth, we constructed an aligned, lattice-mismatched, rectangular moiré heterostructure, that is, Bi(110)-SnSe(001), which intrinsically hosts 1D-EFBs localized by the lattice-mismatch-induced 1D BR structures. The stripe-like BR structures develop in the *ZZ* direction, at which the boundaries of two domains with oppositely buckled Bi–Bi dimers meet. In other words, at the two sides of the boundary, the buckling directions of Bi–Bi dimers are topologically inequivalent, which leads to destructive interference between the edge states of the two domains, as we will comprehensively discuss elsewhere.[47] This interference localizes electrons of the 1D-EFBs in the *ZZ* direction, along which the electronic states are extended to form a flat topological band, and confines those electrons within the BR regions along the orthogonal *AC* direction to form a flat atomic band.[46] Therefore, 1D-EFBs are naturally emergent. This discovery allows us to obtain 1D-EFBs in self-aligned untwisted vdW layers, without delicate control of the twist angles between them, which simplifies the process for preparing potential anisotropic correlated electronic states in 2D layers. This strategy for engineering 1D-EFBs is, most likely, extendable to other group IV–VI phosphorene analogues with different lattice mismatches.

4. Experimental Section

Sample Preparation: The high-quality SnSe single crystals used in the experiments were self-grown using the temperature gradient growth method from high purity (99.9999%) Sn and Se granules. First, Sn and Se granules with the stoichiometry of SnSe and a total weight of 30 g were loaded into a quartz ampoule with an inner diameter of 11 mm. Then, the ampoule was evacuated to better than 5×10^{-5} Torr and sealed. The primary ampoule was inserted into a quartz tube, which was evacuated and sealed to protect the sample and ampoule. The double-sealed quartz tube was loaded into a tubular furnace at a 15° angle from the horizontal plane. In the furnace, the sample was slowly heated to 980 °C over 30 h, soaked at this temperature for 48 h, and then cooled from 980 to 500 °C at a precisely controlled rate of 1 °C h⁻¹. After the furnace was cooled to room temperature (RT), the synthesized SnSe single crystals were removed from the quartz ampoule and exposed to the air.

Prior to the Bi growth and STM experiments, the SnSe crystals were cleaved in situ in a preparation chamber under ultrahigh vacuum (UHV) conditions at RT. Bi atoms (99.999% purity, Sigma-Aldrich) were evaporated from a resistively heated evaporator onto the freshly cleaved SnSe surface. The SnSe substrates were kept at RT during the evaporation. The prepared samples were immediately transferred under UHV to the STM chamber and cooled to 5.0 K.

STM Measurements: The STM, AFM, and spectroscopy experiments were conducted using a UHV low-temperature STM system (CreaTec). STM topographic images were acquired in the constant-current mode. The d*I*/d*V* spectra were measured using the standard lock-in technique with a bias modulation of 8–10 mV at 321.333 Hz. The STM tips were made of chemically etched W and were calibrated spectroscopically against the Shockley surface states of cleaned Cu(111) or Au(111) surfaces before measurements were performed on Bi islands/SnSe. For the qPlus AFM measurement, the tip was decorated with CO by picking up a single molecule from an Ag(100) surface. The parameters for picking up CO were as follows: a sample bias of $V_b = 40$ mV and a tunnelling current of $I = 100$ pA. The AFM imaging was performed via frequency modulation with a constant amplitude of $A = 120$ pm. The resonance frequency of the AFM probe was $f_0 = 24.5$ kHz, and its quality factor was $Q = 53 764$.

DFT Calculations: DFT calculations were performed using the generalized gradient approximation for the exchange-correlation potential with a plane-wave basis and the projector augmented wave method, as implemented in the Vienna Ab initio Simulation Package.[48–50] The supercell for modelling the Bi/SnSe interface consisted of an 11×11 2-AL Bi(110) layer and a 12×12 2-AL SnSe layer, containing 1060 atoms in total. A 15 Å vacuum layer was adopted to avoid image interactions. The Γ point was used for sampling the first Brillouin zone in structural relaxation and DOS calculations. The energy cutoff for the structural relaxation and electronic structure calculations of the superlattice was set as 200 eV. During the optimization of the Bi–SnSe superlattice, the bottom SnSe layer was kept fixed, and all other atoms were fully relaxed until the residual force per atom was <0.05 eV Å^{-1}. In the structural relaxation and electronic property calculations, Grimme's D3 form vdW correction was applied with the Perdew Burke Ernzerhof (PBE) exchange functional (PBE-D3).[51,52] All the electronic properties of the superlattice were calculated with consideration of spin-orbit coupling.

Supporting Information

Supporting Information is available from the Wiley Online Library or from the author.

Conflict of Interest

The authors declare no conflict of interest.

Data Availability Statement

The data that support the findings of this study are available from the corresponding author upon reasonable request

[1] C. R. Dean, L. Wang, P. Maher, C. Forsythe, F. Ghahari, Y. Gao, J. Katoch, M. Ishigami, P. Moon, M. Koshino, T. Taniguchi, K. Watanabe, K. L. Shepard, J. Hone, P. Kim, *Nature* **2013**, *497*, 598.

[2] Y. Cao, V. Fatemi, A. Demir, S. Fang, S. L. Tomarken, J. Y. Luo, J. D. Sanchez-Yamagishi, K. Watanabe, T. Taniguchi, E. Kaxiras, R. C. Ashoori, P. Jarillo-Herrero, *Nature* **2018**, *556*, 80.

[3] E. C. Regan, D. Wang, C. Jin, M. I. Bakti Utama, B. Gao, X. Wei, S. Zhao, W. Zhao, Z. Zhang, K. Yumigeta, M. Blei, J. D. Carlstrom, K. Watanabe, T. Taniguchi, S. Tongay, M. Crommie, A. Zettl, F. Wang, *Nature* **2020**, *579*, 359.

[4] Y. Tang, L. Li, T. Li, Y. Xu, S. Liu, K. Barmak, K. Watanabe, T. Taniguchi, A. H. MacDonald, J. Shan, K. F. Mak, *Nature* **2020**, *579*, 353.

[5] P. Wang, G. Yu, Y. H. Kwan, Y. Jia, S. Lei, S. Klemenz, F. A. Cevallos, R. Singha, T. Devakul, K. Watanabe, T. Taniguchi, S. L. Sondhi, R. J. Cava, L. M. Schoop, S. A. Parameswaran, S. Wu, *Nature* **2022**, *605*, 57.

[6] Z. Wang, D. A. Rhodes, K. Watanabe, T. Taniguchi, J. C. Hone, J. Shan, K. F. Mak, *Nature* **2019**, *574*, 76.

[7] R. Ribeiro-Palau, C. Zhang, K. Watanabe, T. Taniguchi, J. Hone, C. R. Dean, *Science* **2018**, *361*, 690.

[8] H. Yu, G. B. Liu, J. Tang, X. Xu, W. Yao, *Sci. Adv.* **2017**, *3*, e1701696.

[9] Y. Bai, L. Zhou, J. Wang, W. Wu, L. J. McGilly, D. Halbertal, C. F. B. Lo, F. Liu, J. Ardelean, P. Rivera, N. R. Finney, X. C. Yang, D. N. Basov, W. Yao, X. Xu, J. Hone, A. N. Pasupathy, X. Y. Zhu, *Nat. Mater.* **2020**, *19*, 1068.

[10] D. Unuchek, A. Ciarrocchi, A. Avsar, K. Watanabe, T. Taniguchi, A. Kis, *Nature* **2018**, *560*, 340.

[11] X. R. Mao, Z. K. Shao, H. Y. Luan, S. L. Wang, R. M. Ma, *Nat. Nanotechnol.* **2021**, *16*, 1099.

[12] H. Baek, M. Brotons-Gisbert, Z. X. Koong, A. Campbell, M. Rambach, K. Watanabe, T. Taniguchi, B. D. Gerardot, *Sci. Adv.* **2020**, *6*, eaba8526.

[13] M. Yankowitz, S. Chen, H. Polshyn, Y. Zhang, K. Watanabe, T. Taniguchi, D. Graf, A. F. Young, C. R. Dean, *Science* **2019**, *363*, 1059.

[14] Y. Cao, V. Fatemi, S. Fang, K. Watanabe, T. Taniguchi, E. Kaxiras, P. Jarillo-Herrero, *Nature* **2018**, *556*, 43.

[15] Y. Choi, J. Kemmer, Y. Peng, A. Thomson, H. Arora, R. Polski, Y. Zhang, H. Ren, J. Alicea, G. Refael, F. von Oppen, K. Watanabe, T. Taniguchi, S. Nadj-Perge, *Nat. Phys.* **2019**, *15*, 1174.

[16] A. Kerelsky, L. J. McGilly, D. M. Kennes, L. Xian, M. Yankowitz, S. Chen, K. Watanabe, T. Taniguchi, J. Hone, C. Dean, A. Rubio, A. N. Pasupathy, *Nature* **2019**, *572*, 95.

[17] Y. Xie, B. Lian, B. Jack, X. Liu, C. L. Chiu, K. Watanabe, T. Taniguchi, B. A. Bernevig, A. Yazdani, *Nature* **2019**, *572*, 101.

[18] J. Mao, S. P. Milovanović, M. Anđelković, X. Lai, Y. Cao, K. Watanabe, T. Taniguchi, L. Covaci, F. M. Peeters, A. K. Geim, Y. Jiang, E. Y. Andrei, *Nature* **2020**, *584*, 215.

[19] Y. Jiang, X. Lai, K. Watanabe, T. Taniguchi, K. Haule, J. Mao, E. Y. Andrei, *Nature* **2019**, *573*, 91.

[20] M. H. Naik, M. Jain, *Phys. Rev. Lett.* **2018**, *121*, 266401.

[21] K. Slagle, L. Fu, *Phys. Rev. B* **2020**, *102*, 235423.

[22] L. Wang, E. M. Shih, A. Ghiotto, L. Xian, D. A. Rhodes, C. Tan, M. Claassen, D. M. Kennes, Y. Bai, B. Kim, K. Watanabe, T. Taniguchi, X. Zhu, J. Hone, A. Rubio, A. N. Pasupathy, C. R. Dean, *Nat. Mater.* **2020**, *19*, 861.

[23] F. Wu, T. Lovorn, E. Tutuc, A. H. MacDonald, *Phys. Rev. Lett.* **2018**, *121*, 026402.

[24] Z. Zhang, Y. Wang, K. Watanabe, T. Taniguchi, K. Ueno, E. Tutuc, B. J. LeRoy, *Nat. Phys.* **2020**, *16*, 1093.

[25] H. Li, S. Li, M. H. Naik, J. Xie, X. Li, J. Wang, E. Regan, D. Wang, W. Zhao, S. Zhao, S. Kahn, K. Yumigeta, M. Blei, T. Taniguchi, K. Watanabe, S. Tongay, A. Zettl, S. G. Louie, F. Wang, M. F. Crommie, *Nat. Mater.* **2021**, *20*, 945.

[26] W. M. Zhao, L. Zhu, Z. Nie, Q. Y. Li, Q. W. Wang, L. G. Dou, J. G. Hu, L. Xian, S. Meng, S. C. Li, *Nat. Mater.* **2022**, *21*, 284.

**ADVANCED
SCIENCE NEWS**

www.advancedsciencenews.com

**ADVANCED
MATERIALS**

www.advmat.de

[27] L. Xian, D. M. Kennes, N. Tancogne-Dejean, M. Altarelli, A. Rubio, *Nano Lett.* **2019**, *19*, 4934.

[28] A. Yazdani, *Science* **2021**, *371*, 1098.

[29] E. Y. Andrei, D. K. Efetov, P. Jarillo-Herrero, A. H. MacDonald, K. F. Mak, T. Senthil, E. Tutuc, A. Yazdani, A. F. Young, *Nat. Rev. Mater.* **2021**, *6*, 201.

[30] D. M. Kennes, L. Xian, M. Claassen, A. Rubio, *Nat. Commun.* **2020**, *11*, 1124.

[31] L. Zhang, X. Zhang, G. Lu, *Chem. Mater.* **2021**, *33*, 7432.

[32] L. C. Gomes, A. Carvalho, *Phys. Rev. B* **2015**, *92*, 085406.

[33] X. Ling, H. Wang, S. Huang, F. Xia, M. S. Dresselhaus, *Proc. Natl. Acad. Sci. U. S. A.* **2015**, *112*, 4523.

[34] H. Guo, X. Cui, W. Zhou, D. Han, C. Lin, L. Cao, M. Feng, *J. Appl. Phys.* **2018**, *124*, 045301.

[35] G. Duvjir, T. Min, T. T. Ly, T. Kim, A.-T. Duong, S. Cho, S. H. Rhim, J. Lee, J. Kim, *Appl. Phys. Lett.* **2017**, *110*, 262106.

[36] S.-u. Kim, A.-T. Duong, S. Cho, S. H. Rhim, J. Kim, *Surf. Sci.* **2016**, *651*, 5.

[37] Z. Wang, C. Fan, Z. Shen, C. Hua, Q. Hu, F. Sheng, Y. Lu, H. Fang, Z. Qiu, J. Lu, Z. Liu, W. Liu, Y. Huang, Z. A. Xu, D. W. Shen, Y. Zheng, *Nat. Commun.* **2018**, *9*, 47.

[38] P. J. Kowalczyk, O. Mahapatra, D. N. McCarthy, W. Kozlowski, Z. Klusek, S. A. Brown, *Surf. Sci.* **2011**, *605*, 659.

[39] L. Peng, J. Qiao, J. J. Xian, Y. Pan, W. Ji, W. Zhang, Y. S. Fu, *ACS Nano* **2019**, *13*, 1885.

[40] X. Dong, Y. Li, J. Li, X. Peng, L. Qiao, D. Chen, H. Yang, X. Xiong, Q. Wang, X. Li, J. Duan, J. Han, W. Xiao, *J. Phys. Chem. C* **2019**, *123*, 13637.

[41] Y. Lu, W. Xu, M. Zeng, G. Yao, L. Shen, M. Yang, Z. Luo, F. Pan, K. Wu, T. Das, P. He, J. Jiang, J. Martin, Y. P. Feng, H. Lin, X. S. Wang, *Nano Lett.* **2015**, *15*, 80.

[42] P. J. Kowalczyk, S. A. Brown, T. Maerkl, Q. Lu, C. K. Chiu, Y. Liu, S. A. Yang, X. Wang, I. Zasada, F. Genuzio, T. O. Mentes, A. Locatelli, T. C. Chiang, G. Bian, *ACS Nano* **2020**, *14*, 1888.

[43] D. Waters, Y. Nie, F. Lupke, Y. Pan, S. Folsch, Y. C. Lin, B. Jariwala, K. Zhang, C. Wang, H. Lv, K. Cho, D. Xiao, J. A. Robinson, R. M. Feenstra, *ACS Nano* **2020**, *14*, 7564.

[44] M. Morgenstern, *Surf. Rev. Lett.* **2012**, *10*, 933.

[45] Y. Pan, S. Folsch, Y. Nie, D. Waters, Y. C. Lin, B. Jariwala, K. Zhang, K. Cho, J. A. Robinson, R. M. Feenstra, *Nano Lett.* **2018**, *18*, 1849.

[46] N. Regnault, Y. Xu, M. R. Li, D. S. Ma, M. Jovanovic, A. Yazdani, S. S. P. Parkin, C. Felser, L. M. Schoop, N. P. Ong, R. J. Cava, L. Elcoro, Z. D. Song, B. A. Bernevig, *Nature* **2022**, *603*, 824.

[47] D. P. Guo, In preparation.

[48] P. E. Blöchl, *Phys. Rev. B* **1994**, *50*, 17953.

[49] G. Kresse, J. Furthmüller, *Phys. Rev. B* **1996**, *54*, 11169.

[50] G. Kresse, D. Joubert, *Phys. Rev. B* **1999**, *59*, 1758.

[51] S. Grimme, J. Antony, S. Ehrlich, H. Krieg, *J. Chem. Phys.* **2010**, *132*, 154104.

[52] J. P. Perdew, K. Burke, M. Ernzerhof, *Phys. Rev. Lett* **1996**, *77*, 3865.